



Cite this: *Lab Chip*, 2021, **21**, 2605

Optimizing pressure-driven pulsatile flows in microfluidic devices†

Steffen M. Recktenwald, ^{*a} Christian Wagner ^{ab} and Thomas John ^a

Unsteady and pulsatile flows receive increasing attention due to their potential to enhance various microscale processes. Further, they possess significant relevance for microfluidic studies under physiological flow conditions. However, generating a precise time-dependent flow field with commercial, pneumatically operated pressure controllers remains challenging and can lead to significant deviations from the desired waveform. In this study, we present a method to correct such deviations and thus optimize pulsatile flows in microfluidic experiments using two commercial pressure pumps. Therefore, we first analyze the linear response of the systems to a sinusoidal pressure input, which allows us to predict the time-dependent pressure output for arbitrary pulsatile input signals. Second, we explain how to derive an adapted input signal, which significantly reduces deviations between the desired and actual output pressure signals of various waveforms. We demonstrate that this adapted pressure input leads to an enhancement of the time-dependent flow of red blood cells in microchannels. The presented method does not rely on any hardware modifications and can be easily implemented in standard pressure-driven microfluidic setups to generate accurate pulsatile flows with arbitrary waveforms.

Received 21st December 2020,
Accepted 7th May 2021

DOI: 10.1039/d0lc01297a

rsc.li/loc

1 Introduction

Pulsatile flows are ubiquitous in nature and technology. In microfluidic devices, pulsatile or oscillatory driving of the flow enhances a broad range of operations and is also used for biomimicry in physiological studies.^{1,2} The inherent time-dependency of velocity, shear stress, and pressure in such flows plays a pivotal advantage in a variety of microfluidic applications, such as mixing,^{3–5} droplet generation,^{6–8} clog mitigation, and filtration of circulating tumor cells from whole blood,⁹ in bioassays,¹⁰ and for particle manipulation.^{11–13} Additionally, due to their potential to improve the growth and viability of mechanosensitive cells, pulsatile flows are used in bioreactors for regenerative tissue engineering and to enhance microfluidic cell culture efficacy.^{14,15} Moreover, pulsatile flows play a crucial role in biological processes, foremost in the cardiovascular system that transports blood through the body, driven by the pulsatile heartbeat. Here, mimicking hemodynamic conditions in pulsatile blood flow is essential to understand cardiovascular diseases, and recent studies have shown that unsteady driving can give rise to unique nonlinear

hydrodynamic instabilities and turbulence in pulsating flows.^{16,17}

Therefore, precise control of the time-dependent flow field in microfluidic experiments is paramount. To drive a pulsatile flow in microfluidic channels, different generation mechanisms exist, including active, passive, external, and on-chip strategies.^{1,2} Sophisticated microfluidic setups with surface acoustic wave-driven flow chambers¹⁸ or complex cardiac-like flow generators¹⁹ have been used to examine the response of cells in pulsatile microscale flows. However, to generate pulsatile or oscillatory flows in microfluidic systems, most studies rely on commercially available pumps or pressure controllers. Most of such pneumatically operated pressure pumps can be programmed to generate arbitrary pressure waveforms. Nevertheless, they often produce significant deviations from the desired waveform, including overshoots at sudden pressure changes and long response times due to the internal pressure regulation of the controller. These effects can render the generation of hemodynamic and physiologically relevant flow conditions void and hence often limit the application of commercial pressure controllers in experimental investigations.

In this study, we present a software-based approach to overcome such limitations and to achieve an optimized pulsatile flow in pressure-driven microfluidic systems. Therefore, we use two commercially available pressure controllers. In the standard operation mode, these devices generate significant deviations between the desired and

^a Dynamics of Fluids, Department of Experimental Physics, Saarland University, Saarbrücken, Germany. E-mail: steffen.recktenwald@uni-saarland.de

^b Physics and Materials Science Research Unit, University of Luxembourg, Luxembourg

† Electronic supplementary information (ESI) available: One PDF containing additional experimental data and a MATLAB code, which contains the optimization procedure. See DOI: 10.1039/d0lc01297a



actual output pressure signals. While one system shows overshoots and undershoots, the other system produces long transients at sudden pressure jumps. Consequently, we introduce a procedure to derive an adapted pressure input, based on the linear response of the systems. Based on two individual parameters of the system, this adapted pressure input results in an optimized pressure output for both controllers and for various pulsatile waveforms, which significantly improves the time-dependent flow in microfluidic channels. Those setup-dependent parameters are derived for two distinct microfluidic devices from the system response to a sinusoidal driving at various frequencies. We show that the system characteristics mainly depend on the used pressure controller. Hence, for a given pump, the system parameters have to be determined once and can then be used to optimize the time-dependent flow in different microfluidic chips in the same setup. Finally, we employ the optimization technique to study red blood cells (RBCs) in pulsatile microscale flows, highly relevant for investigations of cell dynamics and shape transitions in unsteady flows.

2 Experimental

2.1 Microfluidic setup

We use two commercial pressure controllers, the Elveflow OB1-MK3 and the Fluigent Flow-EZ, to drive fluid through a microfluidic device. Both pressure devices have been used in various microfluidic studies^{11,12,20-23} and are referred to as OB1 pump and as Flow-EZ pump throughout this study. The pressure controller outlet is connected to a 1.5 mL tube containing the fluid sample. Prior to the sample, the time-dependent pressure signal is measured with a differential pressure sensor (NXP MPX5100DP, pressure range 0–1000 mbar) operating at 1 kHz. The sensor voltage signal is recorded over time (National Instruments USB-6009 multi-function DAQ) and converted to millibar. The fluid sample is then pumped through one of three different microfluidic channels. The first microfluidic chip consists of 30 parallel microchannels with a square cross-section of width W and height H of approximately $10 \times 10 \mu\text{m}^2$ and a total length of $L = 40$ mm. The parallel channels are connected at the beginning and end where they share a common fluid inlet and outlet. Further, we use a dividing T-junction as a second channel. Here, the cross-section of the inlet channel has a width $W = 120 \mu\text{m}$, a height of $H = 50 \mu\text{m}$, and a length of $L_{\text{in}} = 30$ mm. The two outlets have a cross-section of $60 \times 50 \mu\text{m}^2$, and a length of $L_{\text{out}} = 15$ mm. While the first two chips are used to characterize the system response, the third device is used for PIV analysis of the time-dependent flow field and contains a single straight channel with a square cross-section of $60 \times 60 \mu\text{m}^2$ and a length of $L \approx 28$ cm. The microfluidic devices are fabricated using polydimethylsiloxane (PDMS, Momentive Performance Materials) through standard soft lithography.²⁴ Inlet and outlet channels are connected with micro medical-grade polyethylene tubing (0.86 mm inner

diameter, Scientific Commodities Inc.) to the sample and waste containers, respectively. The microfluidic device is mounted on an inverted microscope (Nikon Eclipse TE2000-S), equipped with a high-speed camera (Fastec HiSpec 2G) and a LED illumination (Zett Optics ZLED CLS 9000 MV-R). A global trigger signal is used to synchronize the pressure device, the pressure sensor, and the high-speed camera. All experiments are performed at room temperature.

2.2 Flow velocimetry

We employ particle image velocimetry (PIV) in the single-channel device using open-source PIV software.²⁵ The origin of the coordinate system in the x -direction is defined at the channel entry at $L = 0$ and $W/2$ and $H/2$ in y - and z -direction, respectively. We use water as test fluid, seeded with 0.02 wt% of 0.5 μm sized polystyrene particles (Sigma Aldrich), to spatially resolve the velocity profile along the channel width W . A 60 \times oil-immersion objective (Nikon Plan Apo Fluor) with high numerical aperture $\text{NA} = 1.4$ is used to reduce the depth of field. Images are recorded in the middle plane $z = 0$ at $H/2$. Here, the measurement depth δz_m over which particles are detected and contribute to the determination of the velocity field is $\delta z_m/H \approx 0.05$.²⁶

Furthermore, we perform particle tracking velocimetry (PTV) by detecting the movement of individual RBCs in the 30 parallel channels. A 4 \times air objective (Nikon Plan Fluor) with $\text{NA} = 0.13$ is used, which results in the detection of cells in multiple channels and the entire cross-section of the channels ($\delta z_m/H \approx 25$). A self-written MATLAB program is used to detect the positions of individual cells in each image, which are linked over the image sequence and result in individual trajectories. From these trajectories, we determine the individual velocities of the RBCs.

2.3 Red blood cell suspension preparation

Capillary blood is taken with informed consent from healthy voluntary donors and resuspended in phosphate-buffered saline solution (PBS, Gibco). After centrifugation at 1500g for 5 minutes, RBCs are extracted from the sediment and are washed with PBS. This procedure is repeated three times. The final hematocrit concentration of roughly 0.1% Ht is adjusted in a PBS solution, containing 1 mg mL⁻¹ bovine serum albumin (BSA, Sigma Aldrich) to prevent cells from adhering to the inner channel surfaces. Blood withdrawal, preparation, and experiments were performed according to regulations and protocols that were approved by the ethic commission of the 'Aerztekammer des Saarlandes' (reference no 24/12).

3 Results and discussion

3.1 Characterizing the microfluidic systems

Applying a time-depending pressure variation to a commercial pressure controller can lead to significant differences between the set input signal and the actual output pressure, in particular at rapid changes. Here, we



analyze the microfluidic setup that consists of the pressure controller with internal valves and pressure sensors, the tubing, and the connected microfluidic chip. This setup acts as a feedback control system. A schematic representation of the setup and the control system is shown in Fig. 1(a). A widely used general linear feedback control loop for instantaneous regulations is the proportional-integral-derivative (PID) controller. In general, an error value $e(t)$ as the difference between the desired value $r(t)$ and the measured adopted value $y(t)$ is corrected based on proportional, integral, and derivative terms.^{27,28}

To characterize the frequency response of the systems, we apply sinusoidal pressure modulations

$$p_{\text{set}}(t) = p_0 + p_{A,\text{set}} \sin(\omega t), \quad (1)$$

with pressure off-set p_0 , pressure amplitude $p_{A,\text{set}}$, and angular frequency $\omega = 2\pi f$, as desired pressure signal and measure instantaneously the adapted pressure output. These measurements are performed at four pressure off-sets ($p_0 = 50, 100, 250, 500$ mbar) in combination with four amplitudes ($p_{A,\text{set}} = 5, 10, 25, 50\%$ of p_0), covering a broad frequency range of $0.1 \text{ Hz} \leq f \leq 60 \text{ Hz}$. Further, we investigate the frequency response using two distinct microfluidic systems. The first system consists of parallel microchannels, each with a cross-section of roughly $10 \times 10 \mu\text{m}^2$, which are commonly used to study dynamics and shape transitions of RBCs in confined flows.^{29–31} The second system contains a dividing T-junction geometry that is often employed to study partitioning effects of RBCs in bifurcating flows.^{32–34} In this second device, the single inlet channel of the T-junction has a cross-section of $120 \times 50 \mu\text{m}^2$, significantly larger than that of the microchannel chip. A representative result of the frequency response of the microchannel system at $p_0 = 250$ mbar and $p_{A,\text{set}} = 25$ mbar using the Flow-EZ pump is shown in Fig. 2. Here, the desired waveform is shown as gray dashed lines while

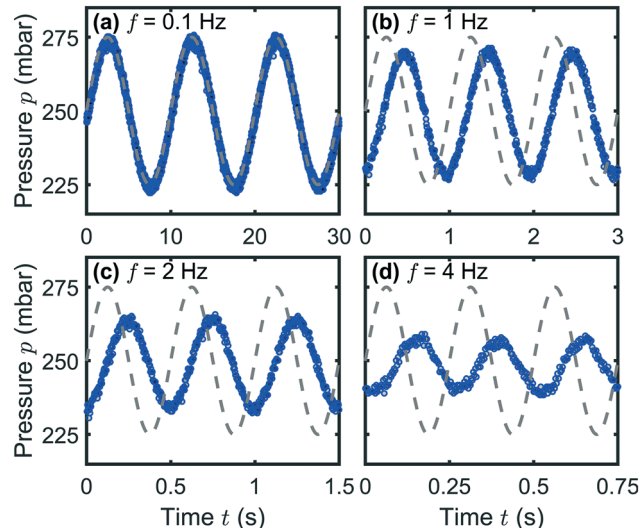


Fig. 2 Sinusoidal pressure modulation at $p_0 = 250$ mbar, $p_{A,\text{set}} = 25$ mbar, and four frequencies f using the Flow-EZ pump in combination with the microchannel device. Gray dashed lines correspond to the set and desired waveform and blue symbols show the measured pressure signal.

the measured sensor signals are plotted as blue symbols. More investigated frequencies for this pressure combination for both pumps are shown in Fig. S1 and S2 in the ESI.[†]

At low frequencies, the system adapts to the set pressure limits during each period without delay and attenuation, as shown for $f = 0.1$ Hz in Fig. 2(a). With increasing frequency, the output signal remains sinusoidal. However, the amplitude p_A of the output pressure signal is attenuated (b-d), with respect to the set amplitude $p_{A,\text{set}}$, and a phase shift φ arises. This deviation continues until only a constant pressure output is generated by the pump above $f \approx 8$ Hz (Fig. S1, ESI[†]). At high frequencies, the pressure signal starts to deviate from the sinusoidal waveform and the system becomes slightly nonlinear, as shown in Fig. 2(d).

The dependence of the pressure amplitude ratio $p_A/p_{A,\text{set}}$ as well as the phase shift φ at not too high frequencies can be described by linear response theory and allows us to characterize the systems, similar to previous microfluidic studies.^{35,36} Fig. 3 shows the representative Bode plots as frequency response at $p_0 = 250$ mbar for both investigated microfluidic systems (a) the microchannels and (b) the dividing T-junction. The left and right columns in (a) and (b) correspond to the Flow-EZ and the OB1 pump, respectively.

At low frequencies in Fig. 3(a), both pumps reach the set amplitude of the pressure modulation, hence $p_A/p_{A,\text{set}} = 1$, as indicated by the horizontal dashed lines. For the Flow-EZ pump, $p_A/p_{A,\text{set}}$ starts to decrease above $f \approx 0.6$ Hz. In contrast, the pressure amplitude ratio for the OB1 pump first increases above $f \approx 4$ Hz and reaches a maximum at $f \approx 20$ Hz. Subsequently, the amplitude ratio decreases until only a constant pressure signal is generated above 40 Hz. We find these characteristic behaviors of the Flow-EZ and the OB1 pump shown in Fig. 3(a) for all investigated pressure offsets p_0 , as shown in the ESI.[†] This shows the linear response

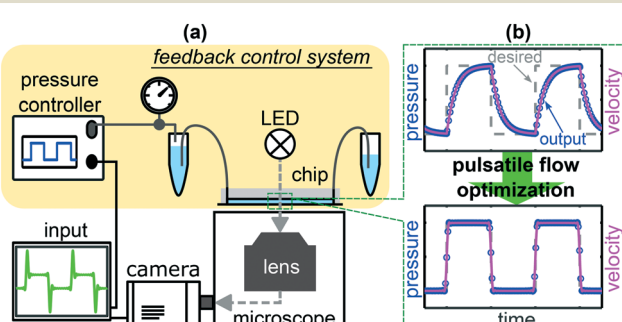


Fig. 1 (a) Schematic representation of the microfluidic setup. The feedback control system consists of the pressure controller and sensor, the tubing, the sample containers, and the microfluidic chip. The effect of the optimization approach is schematically shown in (b). While the non-optimized device output pressure deviates from the desired waveform (top), the optimization approach enhances the time-dependent pressure output and hence the flow velocity in the microfluidic chip (bottom).



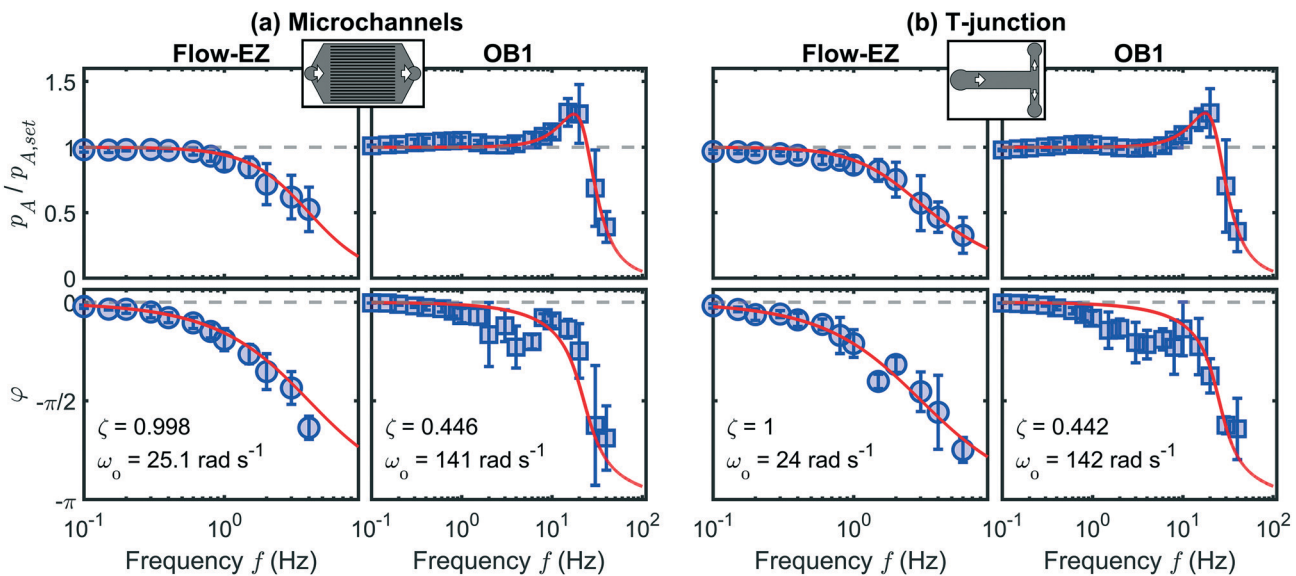


Fig. 3 Pressure amplitude ratio $p_A / p_{A,\text{set}}$ (top) and phase shift φ (bottom) at $p_0 = 250$ mbar as a function of frequency f for (a) the microchannel system and (b) the dividing T-junction, as indicated by the schematic drawings in the top row. The left and right columns in (a) and (b) correspond to the Flow-EZ and the OB1 pump, respectively. Error bars correspond to averaging over different pressure amplitudes ($5\% \leq p_{A,\text{set}} \leq 50\%$ of p_0). Red lines show the fit according to eqn (4) and (5) using the parameters in (a) and (b).

of the systems up to high frequencies and amplitudes depending on the used pressure controller, as shown in Fig. 3. Additionally, we do not observe any significant influence of the two distinct microfluidic systems on the frequency response, shown in Fig. 3(a) and (b). Hence, the described approach can be used to initially determine the transmission characteristics of a standard microfluidic setup, consisting of a pressure controller, sample container, tubing, and an arbitrary microfluidic chip. These characteristics can subsequently be used to optimize the pulsatile flow in other microfluidic channels connected to the same pressure controller, sample container, and tubing.

For both microfluidic chips, the differences in the pressure regulation between both pumps arise due to different internal control parameters. When setting a time-dependent pressure signal $p_{\text{set}}(t)$, the devices use a PID algorithm to adapt the continuously measured pressure to the actual set value. This response of the systems $p(t)$, which is the pump and the attached microfluidic chip can be modeled by a second-order differential equation, similar to a driven damped harmonic oscillator^{27,28}

$$\ddot{p}(t) + 2\zeta\omega_0\dot{p}(t) + \omega_0^2p(t) = \omega_0^2p_{\text{set}}(t), \quad (2)$$

with the damping constant ζ and the undamped angular frequency ω_0 . For the particular system considered here, the output pressure $p(t)$ must be identical to the set pressure $p_{\text{set}}(t)$ in the limit of very slow variation of the set signal. This low-frequency limit corresponds to the elimination of the time derivative in eqn (2). Therefore, the two system-dependent constants ζ and ω_0 completely characterize the linear response of the systems, in contrast to the three constants for a general PID controlled system. For a

sinusoidal excitation in eqn (1) with an angular frequency ω and an amplitude $p_{A,\text{set}}$, the solution of eqn (2) is

$$p(t) = p_0 + a(\omega)p_{A,\text{set}} \sin(\omega t + \varphi(\omega)) \quad (3)$$

with

$$a(\omega) = \frac{\omega_0^2}{\sqrt{(2\omega_0\zeta\omega)^2 + (\omega^2 - \omega_0^2)^2}}, \quad (4)$$

$$\varphi(\omega) = \arctan \frac{2\omega_0\zeta\omega}{\omega_0^2 - \omega^2} + n\pi, \varphi \in [-\pi, 0]. \quad (5)$$

We use this solution to fit the frequency response, shown as red lines in Fig. 3, and extract the system coefficients ζ and ω_0 (see ESI†). In general, when $\zeta > 1$ the system is overdamped and the pressure signal reaches the steady equilibrium state at a step response without oscillating. For damping ratios smaller than unity $\zeta < 1$, the system is underdamped and oscillates with a gradually decreasing amplitude at sudden changes in the pressure signal. In the case of the underdamped system, we determine the resonance frequency $f_r = \omega_0 \sqrt{1 - 2\zeta^2} / (2\pi) = 20$ Hz at which the amplitude is maximal for the OB1 pump as shown in Fig. 3.

The solution of eqn (3) enables us to predict the system response to arbitrary excitation waveforms. Furthermore, we calculate an adapted, optimized system input to achieve the desired output pressure waveform. Therefore, we expand an arbitrary set pressure waveform with period T into a finite complex Fourier series. A common problem with finite Fourier series expansion is the so-called Gibbs phenomenon, which leads to ringing at jump discontinuities, e.g., for a rectangular waveform. Here, we use a σ -approximation to reduce this ringing effect³⁷ with the Lanczos σ -factor. This

modification of the Fourier series for an arbitrary set pressure waveform leads to

$$p_{\text{set}}^{\sigma}(t) = \sum_{k=-(k_{\max}-1)}^{k_{\max}-1} p_k^{\sigma} e^{i\omega_k t}, \quad \omega_k = \frac{2\pi k}{T} \quad (6)$$

with

$$p_k^{\sigma} = \frac{\sigma_k}{T} \int_0^T p_{\text{set}}(t) e^{i\omega_k t} dt, \quad \sigma_k = \text{sinc}\left(\frac{k}{k_{\max}}\right) \quad (7)$$

as the complex coefficients p_k^{σ} , the maximum number of harmonics $k_{\max} - 1$, and in particular for $k = 0$ the pressure offset p_0 . This series can also be expressed with real-valued coefficients based on sine and cosine functions (ESI†). For commonly used waveforms, *e.g.*, rectangular, triangular, and sawtooth, the coefficients are tabulated in standard mathematical textbooks. For the waveforms used in this study, the corresponding Fourier series approximations are given in the ESI.† For arbitrary waveforms, such as the blood pressure waveform in an artery, the coefficients must be calculated by numerical integration. To facilitate the coefficient determination for arbitrary signals, we included a corresponding MATLAB script in the ESI.†

3.2 Pressure output prediction and input optimization

The characterization of the system response to a sinusoidal driving enables us to predict the pressure regulation for arbitrary pressure modulations. Using the Fourier decomposition of the set pressure in eqn (6) and the analytic solution of the model eqn (3), we can predict the pressure output

$$p(t) = \sum_{k=-(k_{\max}-1)}^{k_{\max}-1} a(\omega_k) p_k^{\sigma} e^{i[\omega_k t + \varphi(\omega_k)]}. \quad (8)$$

A representative result for the prediction of the pump response to a rectangular input pressure waveform is shown in Fig. 4(a) and (b) for the Flow-EZ pump and (b) for the OB1 pump. The input signals are plotted as gray dashed lines. The measured pressure signals are shown as blue symbols and the predicted responses are plotted as dotted red lines.

Fig. 4(a) and (b) demonstrate the pressure response due to internal PID regulations in the case of an abruptly changing input signal for the Flow-EZ and OB1 pump, respectively. The system in (a) is overdamped and the pump responds to the sudden increase or decrease in the set pressure by slowly approaching the pressure limits at $p_0 \pm p_A$. In contrast, the system in (b) is underdamped and reacts faster to the abrupt change of the input signal, but generates overshoots and undershoots at the rising and falling edges of the set signal, respectively. This behavior is captured by the pressure predictions. In both cases, the predictions are in good agreement with the measured response. The response and predictions to other waveforms are shown in the ESI.†

Based on the linearity of the system, we can precalculate the required set pressure to achieve the desired output

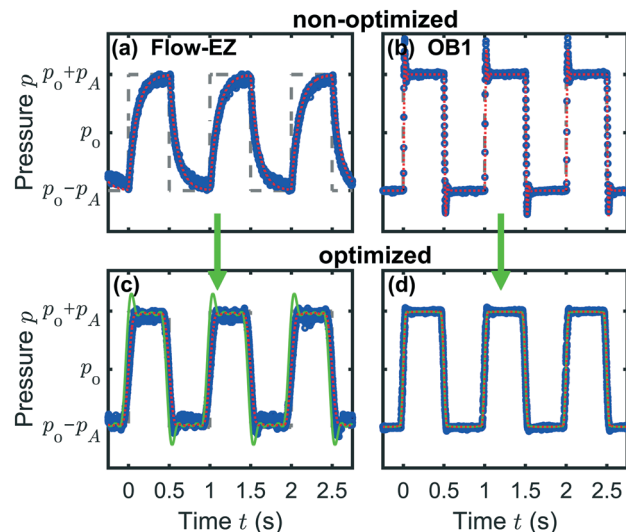


Fig. 4 Rectangular pressure waveform at a frequency of $f = 1$ Hz for (a) the Flow-EZ pump at $p_0 = 60$ mbar and $p_A = 10$ mbar, and (b) the OB1 pump at $p_0 = 625$ mbar and $p_A = 125$ mbar. Blue symbols show the pressure signal measured by the pressure sensor and red dotted lines indicate the predicted response. Panel (c) and (d) show the results of the pressure optimization with an adapted input indicated by the green lines.

waveform. The amplitude modulation and phase shift by the system is a convolution and the corresponding deconvolution corrects those modulations and phase shifts.³⁸ This finally leads to the adapted input signal

$$p_{\text{set}}^{\text{opt}}(t) = \sum_{k=-(k_{\max}-1)}^{k_{\max}-1} \frac{p_k^{\sigma}}{a(\omega_k)} e^{i[\omega_k t - \varphi(\omega_k)]}, \quad (9)$$

which results in an optimized output pressure by the system. The coefficients p_k^{σ} are calculated based on the desired output waveform using the Fourier series with sigma approximation in eqn (6). Green arrows highlight the usage of this adapted input in the subsequent figures. Examples for the optimization for both investigated devices are shown in Fig. 4(c) and (d), where the desired pressure output was again the challenging rectangular waveform. Usually, only a few series terms are required to reconstruct the desired waveform, $k_{\max} = 10$ and $k_{\max} = 20$ in Fig. 4(c) and (d), respectively. However, the generation of a rectangular output signal is difficult, because it contains jump discontinuities. In Fig. 4(c) the precalculated overshoots and undershoots in the adapted pressure input, shown as a green line, yield an almost instantaneous adaption to the desired constant pressure during a half period for the rectangular waveform. Similarly, for Fig. 4(d) the overshoots and undershoots in the pressure output are prevented using the precalculated optimized signal input. The adaption results for other waveforms are shown in the ESI.† Moreover, a detailed MATLAB code used to calculate the adapted pressure input for various pulsatile signals is included in the ESI.† to facilitate a straightforward application of the optimization technique.



Although the adapted pressure input results in a reduction of the overshoots and undershoots for the underdamped system, the approximation by a Fourier series can lead to a smoothing of discontinuities, *i.e.*, the edges of the rectangular signal. This effect is shown for a broad range of lengths of the Fourier summation in the ESI.† Thus, the length of the Fourier summation has to be taken into account when applying the adapted pressure method to a signal with sudden pressure jumps.

Finally, we apply this optimization method to a more sophisticated, temporal asymmetric, hemodynamic pressure modulation. Here, a blood pressure waveform in the femoral artery³⁹ is set as an input signal to the Flow-EZ pump, as shown by the gray dashed line in Fig. 5(a). This waveform is characterized by a first systolic phase with a rapid increase in pressure up to a first peak, followed by a rapid decline. Subsequently, the pressure signal shows a second peak during the diastolic phase after the dicrotic notch. The non-optimized output generated by the pressure device is shown as blue symbols in Fig. 5(a). Here, the set systolic peak pressure is not reached during the cardiac cycle and the waveform is shifted in time. However, when applying the adapted, optimized input signal, as indicated by the green line in Fig. 5(b), we can generate a blood pressure waveform in close agreement with the hemodynamic data, which can be used to study cells in microchannels under physiologically relevant conditions using commercial pressure controllers without additional hardware modifications.

3.3 Pulsatile flow characterization

In this section, we apply the optimization technique to demonstrate the positive impact on the temporal velocity field of red blood cells in microfluidic channels.

The temporal and spatial evolution of the flow field inside the microfluidic channels during a pulsatile pressure signal is examined through PIV and PT measurements. Generally, during experiments in microfluidic devices made of PDMS, the channel walls can be deformed considerably depending

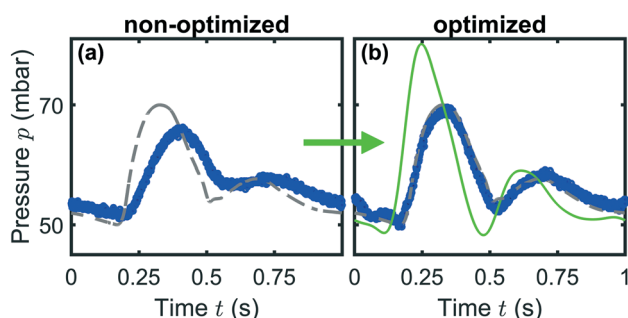


Fig. 5 Blood pressure waveform in the femoral artery during one cardiac cycle of $t \approx 1$ s (a) without and (b) with an adapted pressure input using the Flow-EZ pump. Gray dashed lines correspond to the desired waveform, blue symbols show the measured pressure signal by the pressure sensor and the green line in (b) shows the adapted pressure input.

on the channel dimensions, the PDMS mixture, and the applied pressure drop.^{40–43} To evaluate the deformation of the channel during velocity measurements, we determine the width of a channel with a square cross-section of roughly $10 \times 10 \mu\text{m}^2$ at various positions along the flow direction, and in range of $0 \leq p \leq 1000$ mbar.

When no pressure is applied, the exact width averaged over multiple channels and along the x -direction is $W = 9.57 \pm 0.08 \mu\text{m}$, as shown by the blue line in Fig. S7(a) in the ESI.† Increasing the pressure drop results in a slight increase of the channel width of 3.5% up to $W = 9.90 \pm 0.11 \mu\text{m}$, measured at the channel middle $L = 20$ mm in the x -direction at the highest investigated pressure drop of $p = 1000$ mbar. Further, the channel width widens up to $W = 9.81 \pm 0.14 \mu\text{m}$ at the beginning of the channel at $L = 5$ mm with respect to a position close to channel end with $W = 9.68 \pm 0.19 \mu\text{m}$ at $L = 35$ mm at a pressure drop of $p = 500$ mbar, as exemplified in Fig. S7(b) (ESI†). In this study, velocity measurements are performed in the middle of the channels in x -directions with a maximum pressure amplitude of $\Delta p = 500$ mbar. Hence, we have to consider a maximum channel deformation of roughly 2.2% during the experiments shown here.

To characterize the velocity field during a time-dependent pressure modulation, we perform a PIV analysis of the flow inside a square $60 \times 60 \mu\text{m}^2$ channel. Here, we employ a sinusoidal pressure oscillation with $p_0 = 250$ mbar, $p_A = 50$ mbar, and $f = 0.5$ Hz, as shown in Fig. 6(a). The temporal form of the maximum velocity v_m in the channel center at $W/2$ and $H/2$ is shown as a magenta line in Fig. 6(b) and is in good agreement with an analytical prediction,⁴⁴ indicated by the solid black line. We define the Reynolds number Re , which relates the inertial to viscous forces, as

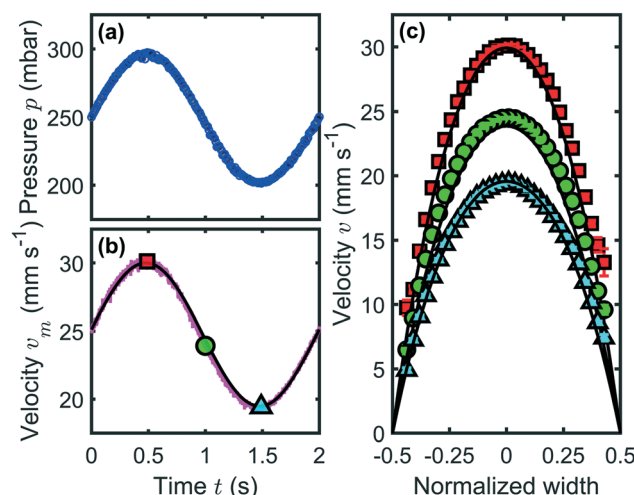


Fig. 6 Analysis of the time-dependent flow inside a $60 \times 60 \mu\text{m}^2$ channel using PIV. (a) Sinusoidal pressure modulation at $p_0 = 250$ mbar, $p_A = 50$ mbar, $f = 0.5$ Hz. (b) Temporal evolution of the maximum velocity in the channel center at $Re \approx 1.8$ and $Wo \approx 0.05$. (c) Spatial velocity profiles at three moments during the cycle as shown by the corresponding symbols in (b). Black solid lines in (b) and (c) correspond to analytical solutions for the velocity inside the channel.



$$\text{Re} = \frac{v_m D_h \rho}{\eta}, \quad (10)$$

with the fluid density ρ , the maximum velocity inside the channel v_m , the fluid viscosity η , and the hydraulic diameter of the microfluidic channel D_h . The hydraulic diameter for a rectangular channel is defined as $D_h = 2WH/(W + H)$. For the data shown in Fig. 6, the Reynolds number is $\text{Re} \approx 1.8$, with $\rho = 1 \text{ g cm}^{-3}$, $v_m = 30 \text{ mm s}^{-1}$, and $\eta = 1 \text{ mPa s}$. During the oscillation cycle, we examine the time-dependency of the spatial flow field at three points in time, indicated by the colored symbols in Fig. 6(b). The corresponding velocity profiles across the normalized channel width are shown in Fig. 6(c).

In pulsatile flows, the dimensionless Womersley number⁴⁵ Wo relates transient inertia effects to viscous forces, according to

$$\text{Wo} = \frac{D_h}{2} \sqrt{\frac{\omega \rho}{\eta}}. \quad (11)$$

For $\text{Wo} \ll 1$, viscous effects dominate the flow and the pulsation frequency is small enough for the steady velocity profile to develop. However, when $\text{Wo} \gg 1$, the transient inertia forces dominate the flow dynamics, which can result in strong deviations of the mean velocity from the Poiseuille flow profile. This effect can lead to flow reversal near the channel walls in pulsatile flows.^{44,46-49} In the experiment shown in Fig. 6, we find $\text{Wo} \approx 0.05$, similar to the flow in arterioles at a heartbeat rate of $f = 2 \text{ Hz}$. Hence, oscillatory inertia forces can be neglected and we observe parabolic flow

profiles that are in good agreement with the analytical predictions, plotted as solid black lines in Fig. 6(c).

As demonstrated in Fig. 4 and 5, commercial pumps fail to produce the desired time-dependent pressure signal in the standard operation mode. Here, we focus on these two distinct waveforms and show how the optimized pressure input improves the time-dependent flow of RBCs inside microfluidic channels. First, we use the challenging rectangular waveform, which in principle provides a versatile instrument to study dynamical shape transitions and relaxation processes of cells and soft, deformable objects in abruptly changing flow fields if overshoots and undershoots or long transient in the pressure signal can be avoided. Second, we use a blood pressure waveform that can be used to study the flow behavior of RBCs, provided that the time-dependent hemodynamic flow conditions are precisely mimicked. The effect of optimized pressure input on the flow of RBCs is shown in Fig. 7(a) and (b) for the rectangular and the blood pressure waveforms, respectively. The left and right columns in (a) and (b) correspond to the non-optimized and the optimized pressure input, respectively.

In Fig. 7(a), a rectangular pressure modulation with $p_0 = 500 \text{ mbar}$, $p_A = 250 \text{ mbar}$, and $f = 0.5 \text{ Hz}$ is applied using the OB1 pump. For the non-optimized case in (a), the overshoots and undershoots of the signal are clearly visible when the pressure changes abruptly. These effects are reduced when the adapted pressure input is used, as shown in the right panel of Fig. 7(a). During these pressure pulsations, RBCs are tracked in the microchannels and their individual velocities are determined. Based on these

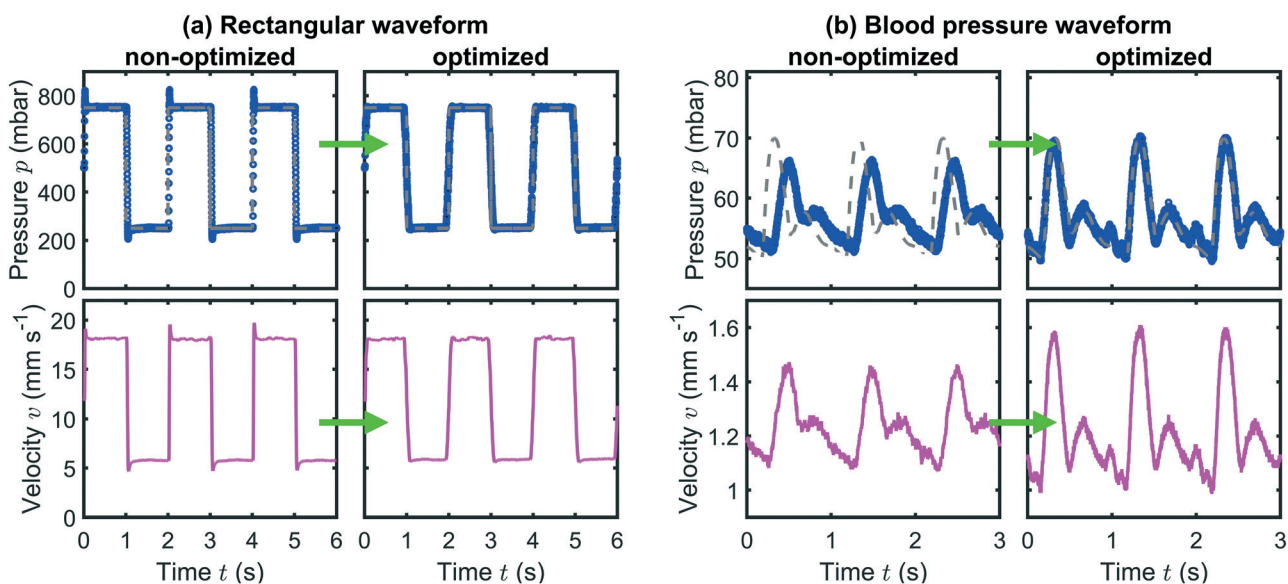


Fig. 7 Tracking of RBCs inside multiple parallel $10 \times 10 \mu\text{m}^2$ channels during (a) a rectangular pressure modulation and (b) a blood pressure waveform. The left and right columns in (a) and (b) show the results without and with the optimized pressure input, respectively. The top panels in (a) show the pressure signals (blue symbols) at $p_0 = 500 \text{ mbar}$, $p_A = 250 \text{ mbar}$, and $f = 0.5 \text{ Hz}$ using the OB1 pump. In (b) the top panels show the pressure signals in the femoral artery with a peak pressure of 70 mbar, a minimum pressure of 50 mbar, and a frequency of $f = 1 \text{ Hz}$, using the Flow-EZ pump. In the bottom panels, the average RBC velocities are shown at $\text{Re} \approx 0.2$ and $\text{Wo} \approx 0.01$, and $\text{Re} \approx 0.01$ and $\text{Wo} \approx 0.01$ for (a) and (b), respectively.



individual velocities, the mean velocity at each point in time is calculated and plotted in the bottom row of Fig. 7. In the case of the non-optimized pressure input, the overshoots and undershoots in the pressure signal are also reflected in the average velocity, because of the small $Re \approx 0.2$. However, applying an adapted pressure input results in a significant reduction of these effects. Due to the small channel dimensions, the pulsatile flow reaches a periodic steady-state immediately after the pulsating pressure signal is applied, in accordance with numerical predictions based on the set pressure waveform.^{46–48} Due to the finite length of the Fourier summation ($k_{\max} = 10$) used to calculate the adapted pressure input in Fig. 7(b), the abrupt pressure jumps and hence the velocity is gradually smoothed, as shown in Fig. S8 (ESI†). Additionally, we observe a small time delay of $\Delta t \approx 8$ ms between the pressure and average velocity signal in Fig. 7, independent of the applied pressure input. Since $Re \ll 1$ and $Wo \ll 1$, the observed time delay does not arise as a consequence of transient inertia forces, as predicted numerically at higher Wo ,^{44,46,48,49} but might be caused by air in the sample container or by any compliance in the setup components.³⁵

In addition to the abruptly changing pressure signal in Fig. 7(a), we further apply a waveform of biological interest in Fig. 7(b). As discussed in Fig. 5, the set systolic peak pressure and thus RBC velocity is not reached during the cycle and the waveform is shifted in time for the non-optimized case in Fig. 7(b). However, applying the optimized approach reduces the time delay and generates a time-dependent pressure and velocity modulation in good agreement with the desired signal.

As exemplified in Fig. 7 for two distinct waveforms, the presented approach can be used to optimize pressure-driven time-dependent flows with arbitrary waveforms. Particularly, the tracking of RBCs in such optimized pulsatile flows provides a versatile platform to study RBC dynamics and shape transitions as a function of the pressure waveform, amplitude, and frequency of the flow modulation. Therefore, the optimized pressure input introduced here can be used in future studies, in an effort to understand how the time scale of the flow couples with the characteristic time scale of single RBCs in capillaries.

4 Conclusions

As microscale pulsatile flows become more important for various microfluidic operations and physiological studies, accurate control of the time-dependent flow conditions is paramount. Therefore, we introduce a software-based optimization approach, which improves the pulsatile pressure output, and thus the microfluidic flow, in a state-of-the-art, pressure-driven microfluidic setup without hardware modifications.

We experimentally probe the amplitude and phase response of two distinct microfluidic systems as a function of frequency to a sinusoidal input for two commercially available pressure controllers and model their distinctive pressure regulation based on a second-order differential equation. This

allows us to predict the pressure output of various pulsatile waveforms, including rectangular, triangular, sawtooth, and arterial blood pressure modulations, which deviate significantly from the desired input waveforms. Further, we show how to generate an adapted pressure input based on a modified Fourier series approximation that results in more accurate pulsatile waveforms. Performing particle tracking velocimetry of red blood cells in microchannels reveals a reduction of unwanted velocity overshoots of a rectangular pressure signal and an enhancement of a hemodynamic waveform when applying the adapted pressure input. Our method can be easily implemented without hardware modifications in commonly used pressure-driven microfluidic setups and provides a relevant tool for studying biological systems in precisely controlled pulsatile microscale flows.

Author contributions

SMR conducted the experiments, acquired and analyzed data, and wrote the manuscript. SMR and TJ conceptualized the optimization method. SMR, TJ, and CW discussed and interpreted data. TJ and CW reviewed and edited the manuscript.

Conflicts of interest

There are no conflicts to declare.

Acknowledgements

This work was supported by the Deutsche Forschungsgemeinschaft DFG in the framework of the research unit FOR 2688 ‘Instabilities, Bifurcations and Migration in Pulsatile Flows’ WA 1336/13-1.

References

- 1 C. K. Byun, K. Abi-Samra, Y.-K. Cho and S. Takayama, *Electrophoresis*, 2014, **35**, 245–257.
- 2 B. Dineau, E. Dressaire and A. Sauret, *Small*, 2020, **16**, 1904032.
- 3 J.-H. Tsai and L. Lin, *Sens. Actuators, A*, 2002, **97–98**, 665–671.
- 4 R. A. Truesdell, P. V. Vorobieff, L. A. Sklar and A. A. Mammoli, *Phys. Rev. E*, 2003, **67**, 066304.
- 5 K. Ward and Z. H. Fan, *J. Micromech. Microeng.*, 2015, **25**, 094001.
- 6 K. Chaudhury, S. Mandal and S. Chakraborty, *Phys. Rev. E*, 2016, **93**, 023106.
- 7 C. Zhou, P. Zhu, Y. Tian, X. Tang, R. Shi and L. Wang, *Lab Chip*, 2017, **17**, 3310–3317.
- 8 P. Zhu and L. Wang, *Lab Chip*, 2017, **17**, 34–75.
- 9 Y. Yoon, S. Kim, J. Lee, J. Choi, R.-K. Kim, S.-J. Lee, O. Sul and S.-B. Lee, *Sci. Rep.*, 2016, **6**, 26531.
- 10 C. Zhang, H. Wang and D. Xing, *Biomed. Microdevices*, 2011, **13**, 885–897.
- 11 S. M. McFaul, B. K. Lin and H. Ma, *Lab Chip*, 2012, **12**, 2369.



12 Y. Lee, D.-M. Kim, Z. Li, D.-E. Kim and S.-J. Kim, *Lab Chip*, 2018, **18**, 915–922.

13 J. Lee, S. E. Mena and M. A. Burns, *Sci. Rep.*, 2019, **9**, 1278.

14 Y. S. Morsi, W. W. Yang, A. Owida and C. S. Wong, *J. Artif. Organs*, 2007, **10**, 109–114.

15 D. Du, K. S. Furukawa and T. Ushida, *Biotechnol. Bioeng.*, 2009, **102**, 1670–1678.

16 D. Xu, S. Warnecke, B. Song, X. Ma and B. Hof, *J. Fluid Mech.*, 2017, **831**, 418–432.

17 D. Xu, A. Varshney, X. Ma, B. Song, M. Riedl, M. Avila and B. Hof, *Proc. Natl. Acad. Sci. U. S. A.*, 2020, **117**, 11233–11239.

18 L. Schmid, A. Wixforth, D. A. Weitz and T. Franke, *Microfluid. Nanofluid.*, 2012, **12**, 229–235.

19 H. Chen, J. Cornwell, H. Zhang, T. Lim, R. Resurreccion, T. Port, G. Rosengarten and R. E. Nordon, *Lab Chip*, 2013, **13**, 2999.

20 Y. Chen, H. N. Chan, S. A. Michael, Y. Shen, Y. Chen, Q. Tian, L. Huang and H. Wu, *Lab Chip*, 2017, **17**, 653–662.

21 C. Iss, D. Midou, A. Moreau, D. Held, A. Charrier, S. Mendez, A. Viallat and E. Helfer, *Soft Matter*, 2019, **15**, 2971–2980.

22 A. Abay, S. M. Recktenwald, T. John, L. Kaestner and C. Wagner, *Soft Matter*, 2020, **16**, 534–543.

23 B. R. Mutlu, T. Dubash, C. Dietsche, A. Mishra, A. Ozbey, K. Keim, J. F. Edd, D. A. Haber, S. Maheswaran and M. Toner, *Lab Chip*, 2020, **20**, 1612–1620.

24 J. Friend and L. Yeo, *Biomicrofluidics*, 2010, **4**, 026502.

25 W. Thielicke and E. J. Stamhuis, *J. Open Res. Softw.*, 2014, **2**, 1–10.

26 C. D. Meinhart, S. T. Wereley and M. H. B. Gray, *Meas. Sci. Technol.*, 2000, **11**, 809–814.

27 J. R. Leigh, *Control Theory*, Iet, 2004, vol. 64.

28 J. Bechhoefer, *Rev. Mod. Phys.*, 2005, **77**, 783–836.

29 J. C. A. Cluitmans, V. Chokkalingam, A. M. Janssen, R. Brock, W. T. S. Huck and G. J. C. G. M. Bosman, *BioMed Res. Int.*, 2014, **2014**, 1–9.

30 A. Guckenberger, A. Kihm, T. John, C. Wagner and S. Gekle, *Soft Matter*, 2018, **14**, 2032–2043.

31 A. Saadat, D. A. Huyke, D. I. Oyarzun, P. V. Escobar, I. H. Övreeide, E. S. G. Shaqfeh and J. G. Santiago, *Lab Chip*, 2020, **20**, 2927–2936.

32 E. Kaliviotis, D. Pasias, J. Sherwood and S. Balabani, *Med. Eng. Phys.*, 2017, **48**, 23–30.

33 J. M. Sherwood, J. Dusting, E. Kaliviotis and S. Balabani, *Biomicrofluidics*, 2012, **6**, 024119.

34 J. M. Sherwood, E. Kaliviotis, J. Dusting and S. Balabani, *Biomech. Model. Mechanobiol.*, 2014, **13**, 259–273.

35 R. C. van der Burgt, P. D. Anderson, J. M. den Toonder and F. N. van de Vosse, *Sens. Actuators, A*, 2014, **220**, 221–229.

36 Y.-J. Li, T. Cao and K.-R. Qin, *Microfluid. Nanofluid.*, 2018, **22**, 81.

37 R. Hamming, *Numerical methods for scientists and engineers*, Courier Corporation, 2012.

38 T. John, D. Pietschmann, V. Becker and C. Wagner, *Am. J. Phys.*, 2016, **84**, 752–763.

39 M. Willemet, P. Chowiencyk and J. Alastrauey, *Am. J. Physiol.*, 2015, **309**, H663–H675.

40 T. Gervais, J. El-Ali, A. Günther and K. F. Jensen, *Lab Chip*, 2006, **6**, 500.

41 B. S. Hardy, K. Uechi, J. Zhen and H. Pirouz Kavehpour, *Lab Chip*, 2009, **9**, 935–938.

42 A. Raj and A. K. Sen, *Microfluid. Nanofluid.*, 2016, **20**, 31.

43 A. Raj, P. P. A. Suthanthiraraj and A. K. Sen, *Microfluid. Nanofluid.*, 2018, **22**, 128.

44 R. Blythman, T. Persoons, N. Jeffers, K. Nolan and D. Murray, *Int. J. Heat Fluid Flow*, 2017, **66**, 8–17.

45 J. R. Womersley, *J. Physiol.*, 1955, **127**, 553–563.

46 X. Qi, D. Scott and D. Wilson, *Chem. Eng. Sci.*, 2008, **63**, 2682–2689.

47 K. Haddad, Ö. Ertunç, M. Mishra and A. Delgado, *Phys. Rev. E*, 2010, **81**, 016303.

48 K. S. Kim and M.-S. Chun, *Korea Aust. Rheol. J.*, 2012, **24**, 89–95.

49 R. Blythman, T. Persoons, N. Jeffers and D. Murray, *J. Phys.: Conf. Ser.*, 2016, **745**, 032044.

